Available online at www.sciencedirect.com
SCIENCE DIRECT®
International Journal of Heat and Mass Transfer 47 (2004) 3533–3547
International Journal of HEAT and MASS TRANSFER
www.elsevier.com/locate/ijhmt

Three-dimensional Marangoni convection in electrostatically positioned droplets under microgravity

Y. Huo, B.Q. Li *

School of Mechanical and Materials Engineering, Washington State University, P.O. Box 642920, Pullman, WA 99164-2920, USA

Received 6 June 2003; received in revised form 3 January 2004
Available online 2 April 2004

Abstract

A numerical study of steady-state and transient 3-D Marangoni convection and heat transfer in electrostatically levitated droplets. The analysis is based on the Galerkin finite element solution of the Navier–Stokes and energy equations. Numerical aspects for the computation of surface driven flows in general curvilinear coordinate system are discussed within the framework of finite elements and differential geometry. Results show that for practical microgravity conditions under which the deformation is small, the single and double beam heating arrangements, when placed at the poles or equator plane, produce an approximately axisymmetric flow profile and temperature distribution with the axis of symmetry defined by the line passing through the centers of the laser beam and the droplet. Thus, an axisymmetric model could provide a reasonably good description, and an exact one when the laser beam is placed at a pole or one beam is placed at both poles. When a tetrahedral or octahedral heating arrangement is applied, complex 3-D flow structures occur, which result from interaction of flow motions associated with each laser beam. For the case studied, the tetrahedral heating arrangement does not seem to produce a significant reduction in internal velocity, in contrast to perception, but the temperature is more uniform. This phenomenon is explained by the fact that the 2- and 4-beam arrangements result in a surface temperature gradient of approximately the same magnitude. The six-beam heating placement produces, however, a much more significant reduction in both velocity and temperature non-uniformity. The transient decaying during cooling is characterized by the evolution of both temperature and velocity fields evolve in a rather complex fashion, with the initial stage dominated by the pronounced thermal and flow mixing on the surface layer of a droplet. The strong surface mixing quickly brings out a surface temperature distribution of axisymmetry, while a 3-D structure still prevails inside until much later. The flow reversal is also observed in the droplets that have been heated by 4- or 6-beam lasers during the decay, and there is a spike in velocity and temperature at the time when the flow reversal occurs.

1. Introduction

Electrostatically levitated droplets are widely used for the fundamental study of melt flows during solidification and for the measurement of thermophysical properties of high melting point, highly corrosive materials in microgravity. In an electrostatic levitator, droplets are suspended by the Coulomb forces that are generated by the interaction of charges impressed on the droplets and a static electric field surrounding them. Lord Rayleigh [1], through asymptotic analysis, showed that there exists a threshold value of charges applied to the droplets before they become disintegrated [1]. This threshold limits the size of a droplet that can be levitated in normal gravity condition. In microgravity environment, however, the Coulomb forces are mainly derived from induced charges and the applied electric field and are to confine a liquid droplet at a desired location. This allows a liquid sample of large size to be positioned, which is important for measuring certain physical properties such as interdiffusion coefficients in undercooled binary alloys.

* Corresponding author.
E-mail address: li@mme.wsu.edu (B.Q. Li).

0017-9310/$ - see front matter © 2004 Elsevier Ltd. All rights reserved.
doi:10.1016/j.ijheatmasstransfer.2004.01.021

Nomenclature

a	radius of a sphere
C	geometric coefficient resulting from boundary integral formulation
C_p	heat capacity
E_0	electric field
$E(\kappa)$	elliptical integral of the second kind
$\mathbf{F}$	force vector from numerical formulation
G	Green's function for free space
$\mathbf{G}$, $\mathbf{H}$	global coefficient matrices of BE formulation
H	Gaussian mean curvature
$\hat{i}$	unit vector of ith component
k	thermal conductivity
$K(\kappa)$	elliptical integral of the first kind
Ma	Marangoni number, $Ma = (\partial\gamma/\partial T)(T_{\min} - T_{\max})\rho C_p a_d/\mu k$
$\mathbf{n}(n_r, n_z)$	outward normal, its r and z components
Q	net charge on the droplet
Q_c	critical charge
Q_0	laser beam heat flux constant
$\mathbf{r}$, $\hat{\mathbf{r}}$, r	point vector, unit vector, and r-coordinate
R	distance measured from the center of the unformed droplet
$\mathbf{t}$	tangential vector
T, T_∞, T_r	temperature, temperature of surroundings, reference temperature
$T_{\max}$, $T_{\min}$	maximum and minimum temperatures
ΔT	difference between $T_{\max}$ and $T_{\min}$
$U_{\max}$	maximum velocity
$\mathbf{u}$	velocity
$\hat{z}$	unit vector of z-direction
z	z-coordinate
z_c	center of mass along the z-axis

Greek symbols

β	thermal expansion coefficient
ε_0	permittivity of free surface or region designated by Ω_2
ε	emissivity
∇	gradient operator
ϕ	shape function
Φ	electric potential
γ	surface tension
κ	geometric parameter for elliptical functions
η	molecular viscosity
ρ	density
θ	θ-direction
σ	electrical conductivity
σ_e	surface charge distribution
σ_s	Stefan–Boltzmann constant
$\bar{\sigma}$	stress tensor
Ω	computational domain

Subscripts

d	droplet
i	the ith point
l	laser beam
1	region inside the droplet
2	region outside the droplet

Superscripts

i	the ith component
T	matrix transpose

One major advantage of electrostatic levitation is that in principle it can be applied to a very wide range of materials including metals, insulators and semiconductors. This is in sharp contrast with the widely used electromagnetic levitation process, developed on the basis of the Faraday's induction principle, which applies only to electrically conducting samples. A more detailed comparison of these two techniques as applied to levitate solid/liquid samples is discussed in a recent publication [10].

In planning space experiments with electrostatically levitated droplets, information on the free surface deformation and transport phenomena such as fluid flow and heat and mass transfer is required. Unlike the electromagnetic levitation systems where strong stirring in a droplet occurs as a result of induced Lorentz forces, electrostatic forces do not produce an internal force in droplets that are electrically conducting such as metals and semiconductor melts. In such a conducting droplet positioned in an electrostatic field, internal flow comes from other sources, among which the surface tension driven flow plays a dominant role. There are both advantages and disadvantages associated with internal flows. In some respects, an internal flow pollutes the measurements of surface tension and viscosity and needs to be suppressed or eliminated as far as the thermophysical property measurement is concerned. In other respects, a strong internal flow may be useful in obtaining certain types of microstructures of materials that solidify under a deep undercooling condition [8]. One technique widely used in microgravity for determining surface tension is to measure the frequency of the free surface oscillation of a free droplet. A free surface oscillation is made possible by first deforming the droplet by an external force and subsequently releasing the force [9]. The surface of a droplet may also be made oscillate by modulating the potentials in the electrodes until the resonant frequency is achieved [8].

Study of the behavior of an electrically charged droplet has been a subject of long history and new and emerging applications with the droplet have provided

continuous thrusts for the research community. Analyses have been carried out on either an inviscid oscillation of charged droplets for simple electric field configuration and shape stability [3–5] or Marangoni convection in the limit of Stokes flow for a sample of a perfect sphericity [7]. Recently, 2-D axisymmetric numerical models have also been developed for Marangoni flows in deformed droplets in electric fields [12]. Droplet experiments indicate that droplet deformation is approximately axisymmetric under a stable levitation condition. While axisymmetric flow models may be useful for axisymmetric laser heating, in reality various non-axisymmetric laser-heating arrangements are also applied, which include single beam, dual beam, and multiple beam heating configurations. These heating arrangements undoubtedly will produce a complex 3-D flow structure that goes far beyond a description by any existing 2-D models. To the best knowledge of the authors, it seems to have very few studies, if any at all, on the 3-D surface tension driven flows in an electrostatically levitated droplet.

This paper presents a 3-D numerical model for Marangoni convection and thermal phenomena associated with an electrostatically positioned droplet in microgravity. The motivation for the work is derived from the need to develop a fundamental understanding of thermal and internal fluid flow fields in these levitated droplets. The free surface deformation is calculated using the hybrid finite/boundary element model published previously [13]. The temperature distribution and fluid flow field in the droplets are calculated using the finite element method. Formulation of surface tension driven flows on a curvilinear surface within the framework of finite elements and differential geometry is discussed. A 3-D finite element simulation of droplet flows represents a computationally intensive task, even with various symmetry (not necessarily axisymmetry) conditions applied to reduce the mesh size for the simulation. To expedite the 3-D computations, the global finite element matrix is sectioned and a special LU solver is designed to account for the changed structure of matrix. Calculations are performed to study both the steady-state and transient evolution of thermal and fluid flow fields in the electrostatically positioned droplets as a function of various commonly used or envisioned laser heating arrangements. The 3-D finite element model, in complement with the 2-D models reported early [13], should be a useful toolkit for developing electrostatic levitation systems for space applications as well as for planning relevant experiments in space shuttle flights or in the International Space Station under construction.

2. Problem statement

Let us consider the problem as illustrated in Fig. 1. An electrically conducting liquid droplet is immersed in a uniform electrostatic field, which is generated by placing two electrodes far apart (Fig. 1(a)). By the principle of electrostatics, a constant potential is established on the surface of the droplet, and surface electric charges are induced so that the electric field inside the droplet is zero. The charge distribution is non-uniform along the surface and, when combined with a self-induced electric field local to the charges, results in a non-uniform electric surface force acting in the outnormal direction [2]. This normal force combines with other surface forces to define the equilibrium shape of the droplet. The internal and tangential surface Maxwell stresses are both zero because the electric potential is constant everywhere inside the droplet by the Gauss law and thus there will be no convection resulting from the electric origin. Laser beams are applied to melt the sample and/or heat it up to a designated temperature. Fig. 1(b) shows a heating arrangement with two laser beams directed at two poles. Various other laser beam arrangements are also considered in this study, including single beam, dual beam, tetrahedral and hexahedral beams. The heating will result in a non-uniform temperature distribution inside the droplet and cause convection if the surface tension of the liquid varies with the surface temperature, as for most metallic and semiconductor melts. Since the laser heating applied here is not necessarily axisymmetric, the surface tension driven flows are bound to be three-dimensional. As shown later, very complex 3-D flow structures and temperature distributions are developed in a droplet for some heating conditions. One important objective of this paper is to develop an understanding of these complex transport phenomena under both steady and transient conditions, which each have specific applications for space materials processing and thermophysical property measurements.

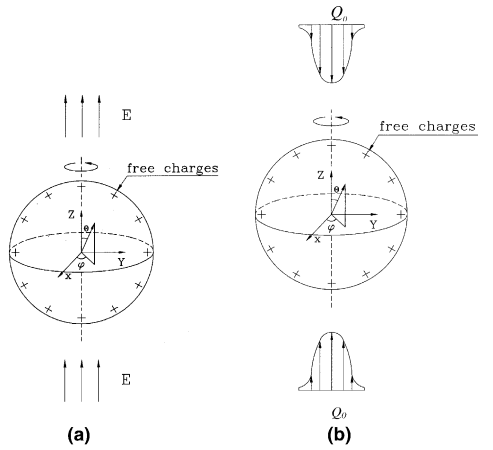

Fig. 1. Schematic representation of a positively charged melt droplet levitated in an electrostatic field: (a) levitation mechanism and (b) a 2-laser-beam heating arrangement.

A complete description of the electrically induced surface deformation and thermally induced fluid flow phenomena in a droplet requires the solution of the coupled Maxwell and Navier–Stokes equations, along with the energy balance equation. However, for metal and semiconductor melts, the electric Reynolds number, $(\varepsilon_0/\sigma)V_{\max}/a$, is on an order of 10^{-16}, which suggests that the convective transport of surface charges (or electric field) may be neglected and the electric field distribution can be calculated as if the liquid droplet were solid [6]. With this, the Maxwell equation is simplified to a partial differential equation governing the distribution of the electric field outside the droplet. The buoyancy effects being neglected for microgravity applications, the equations for the electric, fluid flow and thermal fields may be written as follows:

$$\nabla^2 \Phi = 0 \quad \in \Omega_2 \tag{1}$$

$$\nabla \cdot \mathbf{u} = 0 \quad \in \Omega_1 \tag{2}$$

$$\rho \frac{\partial \mathbf{u}}{\partial t} + \rho \mathbf{u} \cdot \nabla \mathbf{u} = -\nabla p + \nabla \cdot \eta(\nabla \mathbf{u} + (\nabla \mathbf{u})^{\mathrm{T}}) \quad \in \Omega_1 \tag{3}$$

$$\rho C_p \frac{\partial T}{\partial t} + \rho C_p \mathbf{u} \cdot \nabla T = \nabla \cdot k \nabla T \quad \in \Omega_1 \tag{4}$$

The solution of above electric field, fluid flow and heat transfer equations may be obtained by applying the appropriate boundary conditions, which are stated below,

$$\Phi = \Phi_0 \quad \in \Omega_1 \cap \Omega_2 \tag{5}$$

$$\varepsilon_0 \mathbf{n} \cdot \nabla \Phi = -\sigma_e \quad \in \Omega_1 \cap \Omega_2 \tag{6}$$

$$\oint\!\!\!\!\!\!\diamond_{\partial\Omega_1} \sigma_e \, \mathrm{d}s = -\oint\!\!\!\!\!\!\diamond_{\partial\Omega_1} \varepsilon_0 \mathbf{n} \cdot \nabla \Phi \, \mathrm{d}s = Q \quad \in \Omega_1 \cap \Omega_2 \tag{7}$$

$$\Phi = -E_0 R \cos\theta \quad R \to \infty \tag{8}$$

$$-k\mathbf{n} \cdot \nabla T = \varepsilon \sigma_s (T^4 - T_\infty^4) + \mathbf{n} \cdot \hat{\mathbf{r}}_l Q_0 \mathrm{e}^{-r_l^2/a_l^2} \quad \in \Omega_1 \cap \Omega_2 \tag{9}$$

$$\mathbf{u} \cdot \mathbf{n} = 0 \quad \in \Omega_1 \cap \Omega_2 \tag{10}$$

$$\mathbf{n} \cdot \bar{\sigma} \cdot \mathbf{n} + K - \mathbf{n} \cdot \mathbf{T}_E \cdot \mathbf{n} = 2H\gamma \quad \in \Omega_1 \cap \Omega_2 \tag{11}$$

$$\mathbf{t} \cdot \bar{\sigma} \cdot \mathbf{n} = \frac{\mathrm{d}\gamma}{\mathrm{d}T} \mathbf{t} \cdot \nabla T \quad \in \Omega_1 \cap \Omega_2 \tag{12}$$

$$\int_{\Omega_1} \mathrm{d}V = V_0 \quad \in \Omega_1 \tag{13}$$

$$\int_{\Omega_1} z \, \mathrm{d}V = z_c \quad \in \Omega_1 \tag{14}$$

In the above, Eq. (6) is the jump condition for the electric field along the droplet surface, a manifestation of a well known fact that charges are distributed only on the surface of a conducting body. Eq. (8) describes the electric potential condition at infinity. The law of charge conservation is described by Eq. (7), where Q is the total free charge applied on the droplet, which is zero for the problem under consideration for microgravity applications. In Eq. (9), the absorption coefficient is factored into Q_0 and $\hat{\mathbf{r}}_l$ the unit vector of laser beam pointing outward from the origin of the laser, i.e., $\mathbf{n} \cdot \hat{\mathbf{r}}_l \leqslant 0$. Eq. (11) describes the balance of the hydrodynamic, Maxwell and surface tension stresses along the normal direction, which determines the shape of the droplet. The last equation represents the fact that the flow along the surface of the droplet is induced by surface tension force if it is a function of temperature. The constraints of the volume conservation (Eq. (13)) and the center of the mass (Eq. (14)) of the electrostatically levitated droplet are needed to determine the shape and position of the droplet.

It is noted that in the above formulations, the effect of surrounding gas is neglected. The liquid droplet is generally processed under a high vacuum condition, although recently attempts have been made to process in an inert gas environment. For the latter case, it is estimated that the surrounding inert gas contributes about 3% or less to the Marangoni convection.

3. Droplet deformation calculations

In most applications, the droplet deformation is approximately axisymmetric when levitation is stabilized, and thus a 2-D (axisymmetric) model is sufficient to predict the free surface deformation. The computational procedures for electrically induced droplet deformation are detailed in earlier publications [12,13] and thus only a brief summary is outlined here. In essence, the droplet deformation is predicted by a hybrid boundary/finite element method. The numerical model entails the use of boundary elements for electrical potential calculations, while the finite elements are used for free surface deformation calculations. As the free surface shapes are not known a priori, an iterative procedure is required. In principle all discretized equations can be grouped to form a large global sparse matrix equation, which is then solved simultaneously to obtain the electric potential and the free surface shapes. Early numerical simulations showed that under normal conditions considered for both normal and microgravity applications, the droplet deformation is primarily attributed to the Maxwell stress and the viscous stresses due to flow field contributes insignificantly, often less than about 1% [12]. Thus, the flow effect is neglected in the present study.

4. Thermal and fluid flow calculations

With the droplet shape known, the transport equations (Eqs. (2)–(4)) for the thermal and fluid flow fields

along with the boundary conditions are solved using the Galerkin finite element method. The matrix form of the finite element discretized equations for the 3-D model may be written as follows,

$$\begin{bmatrix} \mathbf{M} & 0 & 0 \\ 0 & 0 & 0 \\ 0 & 0 & \mathbf{N}_T \end{bmatrix} \begin{bmatrix} \dot{\mathbf{U}} \\ \dot{\mathbf{P}} \\ \dot{\mathbf{T}} \end{bmatrix} + \begin{bmatrix} \mathbf{A}(\mathbf{U}) + \mathbf{K} & -\mathbf{C} & \mathbf{B} \\ -\mathbf{C}^{\mathrm{T}} & 0 & 0 \\ 0 & 0 & \mathbf{D}_T(\mathbf{U}) + \mathbf{L}_T \end{bmatrix} \begin{bmatrix} \mathbf{U} \\ \mathbf{P} \\ \mathbf{T} \end{bmatrix} = \begin{bmatrix} \mathbf{F} \\ 0 \\ \mathbf{G}_T \end{bmatrix} \tag{15}$$

The coefficient matrices above are defined by

$$\mathbf{M}_p = \int_{\Omega_1} \psi\psi^{\mathrm{T}}\,\mathrm{d}V; \quad \mathbf{N}_T = \int_{\Omega_1} \rho C_p \theta\theta^{\mathrm{T}}\,\mathrm{d}V$$

$$\mathbf{M} = \int_{\Omega_1} \phi\phi^{\mathrm{T}}\,\mathrm{d}V; \quad \mathbf{C}_j = \int_{\Omega_1} \hat{j}\cdot\nabla\phi\psi^{\mathrm{T}}\,\mathrm{d}V$$

$$\mathbf{L}_T = \int_{\Omega_1} k\nabla\theta\cdot\nabla\theta^{\mathrm{T}}\,\mathrm{d}V; \quad \mathbf{A}(\mathbf{U}) = \int_{\Omega_1} \rho\phi\mathbf{u}\cdot\nabla\phi^{\mathrm{T}}\,\mathrm{d}V$$

$$\mathbf{D}_T(\mathbf{U}) = \int_{\Omega_1} \rho C_p\theta\mathbf{u}\cdot\nabla\theta^{\mathrm{T}}\,\mathrm{d}V; \quad \mathbf{B} = \int_{\partial\Omega_1} \frac{\partial\gamma}{\partial T}\mathbf{t}\cdot\nabla\theta^{\mathrm{T}}\,\mathrm{d}S$$

$$\mathbf{G}_T = -\int_{\partial\Omega_1} q_T\theta\,\mathrm{d}s; \quad \mathbf{F} = \int_{\partial\Omega_1} \phi\tau\cdot\mathbf{n}\,\mathrm{d}s$$

$$\mathbf{K}_{ij} = \left(\int_{\Omega_1} \eta\nabla\phi\cdot\nabla\phi^{\mathrm{T}}\,\mathrm{d}V\right)\delta_{ij} + \int_{\Omega_1} \eta(\hat{\imath}\cdot\nabla\phi)(\hat{\jmath}\cdot\nabla\phi^{\mathrm{T}})\,\mathrm{d}V$$

where $j = 1, 2, 3$. Note also that matrix B represents the surface tension effects on the fluid motion. The assembled global matrix equations are stored in the skyline form and solved using the Gaussian elimination method. For the transient calculations, the implicit time scheme is used. The transient term is set to zero for steady-state calculations, however.

5. Computational aspects

Modeling of 3-D surface tension driven flows on a curvilinear surface within the framework of finite elements requires some tedious geometric treatment that involves differential geometry operations and rotation of matrix in local coordinates at the surface for the purpose of appropriately imposing velocity and surface stress boundary conditions (Eqs. (10) and 12). While treatment may vary depending on specific problems, our approach to model the surface driven flow makes use of local surface coordinates and of sharp edges with specified local coordinate system as well as consistent surface normals. With reference to Fig. 2, a local coordinate system (η, ζ, n) is defined at a point on the surface. Note

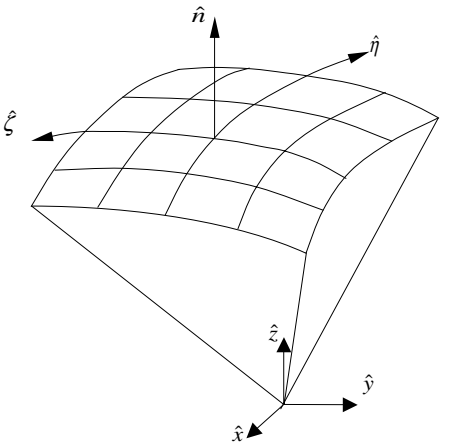

Fig. 2. Transformation between local curvilinear and global Cartesian coordinate systems.

that during calculations this local system may be (although not required) chosen conveniently such that they are coincident with the normalized coordinate systems for isoparametric calculations at the element level. The xyz- and $\eta\zeta n$-coordinate systems are related by the following coordinate transformation,

$$\begin{pmatrix} \frac{\partial}{\partial\eta} \\ \frac{\partial}{\partial\zeta} \\ \frac{\partial}{\partial n} \end{pmatrix} = [J] \begin{pmatrix} \frac{\partial}{\partial x} \\ \frac{\partial}{\partial y} \\ \frac{\partial}{\partial z} \end{pmatrix} = \begin{bmatrix} x_{,\eta} & y_{,\eta} & z_{,\eta} \\ x_{,\zeta} & y_{,\zeta} & z_{,\zeta} \\ x_{,n} & y_{,n} & z_{,n} \end{bmatrix} \begin{pmatrix} \frac{\partial}{\partial x} \\ \frac{\partial}{\partial y} \\ \frac{\partial}{\partial z} \end{pmatrix} \tag{16}$$

In constructing the Jacobian matrix, use has been made of the following differential geometry relations,

$$\mathbf{r}_1 = x_{,\eta}\hat{\imath} + y_{,\eta}\hat{\jmath} + z_{,\eta}\hat{k}, \quad \mathbf{r}_2 = x_{,\zeta}\hat{\imath} + y_{,\zeta}\hat{\jmath} + z_{,\zeta}\hat{k}$$

$$\mathbf{r}_n = \mathbf{r}_1 \times \mathbf{r}_2 = x_{,n}\hat{\imath} + y_{,n}\hat{\jmath} + z_{,n}\hat{k}$$
$$= (y_{,\eta}z_{,\zeta} - z_{,\eta}y_{,\zeta})\hat{\imath} - (x_{,\eta}z_{,\zeta} - z_{,\eta}x_{,\zeta})\hat{\jmath} + (x_{,\eta}y_{,\zeta} - y_{,\eta}x_{,\zeta})\hat{k}$$

The Jacobian matrix may be inverted analytically with the follow result,

$$[J]^{-1} = \frac{1}{|J|}\begin{bmatrix} y_{,\zeta}z_{,n} - z_{,\zeta}y_{,n} & -(y_{,\eta}z_{,n} - z_{,\eta}y_{,n}) & y_{,\eta}z_{,\zeta} - z_{,\eta}y_{,\zeta} \\ -(x_{,\zeta}z_{,n} - z_{,\zeta}x_{,n}) & x_{,\eta}z_{,n} - z_{,\eta}x_{,n} & x_{,\eta}z_{,\zeta} - z_{,\eta}x_{,\zeta} \\ x_{,\zeta}y_{,n} - y_{,\zeta}x_{,n} & -(x_{,\eta}y_{,n} - y_{,\eta}x_{,n}) & x_{,\eta}y_{,\zeta} - y_{,\eta}x_{,\zeta} \end{bmatrix} \tag{17}$$

Furthermore, a shape (or any) function $f(\eta, \zeta)$ defined over the surface is a function of (η, ζ) only and hence $\partial f(\eta, \zeta)/\partial n = 0$. With these relations, one may then relate the volume differential operator to the surface operator,

$$\begin{pmatrix} \dfrac{\partial}{\partial x} \\ \dfrac{\partial}{\partial y} \\ \dfrac{\partial}{\partial z} \end{pmatrix} = [J]^{-1} \begin{pmatrix} \dfrac{\partial}{\partial \eta} \\ \dfrac{\partial}{\partial \zeta} \\ \dfrac{\partial}{\partial n} \end{pmatrix} \tag{18}$$

which may be written in the terminology of differential geometry [14],

$$\begin{aligned} \nabla &= \frac{\partial}{\partial x}\hat{i} + \frac{\partial}{\partial x}\hat{j} + \frac{\partial}{\partial x}\hat{k} \\ &= \frac{1}{H^2}\mathbf{r}_1\left(G\frac{\partial}{\partial \eta} - F\frac{\partial}{\partial \zeta}\right) + \frac{1}{H^2}\mathbf{r}_1\left(E\frac{\partial}{\partial \zeta} - F\frac{\partial}{\partial \eta}\right) \end{aligned} \tag{19}$$

with $E = \mathbf{r}_1^2 = x_{,\eta}^2 + y_{,\eta}^2 + z_{,\eta}^2$, $G = \mathbf{r}_2^2 = x_{,\zeta}^2 + y_{,\zeta}^2 + z_{,\zeta}^2$, $F = \mathbf{r}_1 \cdot \mathbf{r}_2 = x_{,\eta}x_{,\zeta} + y_{,\eta}y_{,\zeta} + z_{,\eta}z_{,\zeta}$ and $H^2 = EG - F^2$. It is stressed that in Eq. (19), (ζ, η) is not necessarily orthogonal so long as they are not collinear. This is important in that irregular quadrilateral surface elements can be readily handled in 3-D finite element calculations presented here.

To perform the calculations, the consistent normal of the surface at node i is required, which must satisfy the continuity equation [15],

$$\begin{aligned} n_x^i &= \frac{1}{n_i}\int_{\Omega_1}\frac{\partial \phi_i}{\partial x}\,\mathrm{d}V, \quad n_y^i = \frac{1}{n_i}\int_{\Omega_1}\frac{\partial \phi_i}{\partial y}\,\mathrm{d}V, \\ n_z^i &= \frac{1}{n_i}\int_{\Omega_1}\frac{\partial \phi_i}{\partial z}\,\mathrm{d}V \end{aligned} \tag{20}$$

where

$$n_i = \left[\left(\int_{\Omega_1}\frac{\partial \phi_i}{\partial x}\,\mathrm{d}V\right)^2 + \left(\int_{\Omega_1}\frac{\partial \phi_i}{\partial y}\,\mathrm{d}V\right)^2 + \left(\int_{\Omega_1}\frac{\partial \phi_i}{\partial z}\right)^2\right]$$

Note that the integration is carried over all the elements sharing node i. Once the normal is known, the two tangential directions $\mathbf{t}_1 = (t_x^1, t_y^1, t_z^1)$ and $\mathbf{t}_2 = (t_x^2, t_y^2, t_z^2)$ can be easily calculated using the cross-product relations, $\mathbf{t}_1 = \mathbf{b} \times \mathbf{n}$, which $\mathbf{b}$ is an arbitrary space vector such that $\mathbf{b} \times \mathbf{n} \neq \mathbf{0}$, and $\mathbf{t}_2 = \mathbf{n} \times \mathbf{b}$. This ensures that the local coordinate system defined by $\mathbf{t}_1 \times \mathbf{t}_2 \times \mathbf{n}$ forms an orthogonal triplet at any node (e.g. node i), a strict condition different from that imposed on (η, ζ, n). The velocities defined in the $\mathbf{t}_1 \times \mathbf{t}_2 \times \mathbf{n}$ system is now related to those in the xyz system through the following transformation,

$$\begin{pmatrix} U_{t_2} \\ U_{t_1} \\ U_n \end{pmatrix} = \begin{bmatrix} t_x^1 & t_y^1 & t_z^1 \\ t_x^2 & t_y^2 & t_z^2 \\ n_x & n_y & n_z \end{bmatrix} \begin{pmatrix} U_x \\ U_y \\ U_z \end{pmatrix} \tag{21}$$

Note that the above transformation also applies to force vectors.

To calculate the surface tension contributions, the integration of ∇ term is first calculated using the relation (Eq. (19)), followed by the above relation to transform the velocities defined in the xyz-coordinates to those in the $\mathbf{t}_1 \times \mathbf{t}_2 \times \mathbf{n}$ system. For the flows under consideration, the normal component of the velocity is zero and the condition can be imposed after the transformation. On the sharp edges formed by the intersection of two surfaces, however, the $\mathbf{t}_1 \times \mathbf{t}_2 \times \mathbf{n}$ system is not uniquely defined by the above computational procedure. This causes difficulty when appropriate velocity and stress boundary conditions are specified along the edge. To overcome the problem, the normal of the edge is taken to be that associated with one of the two joining surfaces and an additional constraint is imposed such that the $\mathbf{t}_1$ is along the edge.

The above treatment in general will give rise to the submatrix $\mathbf{B}$, which, when assembled following standard procedure [12], results in a significant number of unfills in the final global finite element matrix. These unfills may be occupied during LU decomposition and therefore drastically slow down the computations [16]. To reduce these unfills associated with 3-D Marangoni flow computations, the finite element matrix is desectioned such that the terms associated with $\mathbf{B}$ matrix is moved to the right-hand side. As such the matrix $\mathbf{D}_T + \mathbf{A}_L(\mathbf{U})$ may be solved independent of the matrix describing the flow and velocity. Further, making use of the penalty formulation to treat the pressure term eliminates the pressure field. This re-shuffling of the final global matrix elements and unknowns results in savings in both storage space and CPU time required for simulations. Numerical tests show that approximately a factor of 2 to 4 savings in computational time is achieved in the present study, depending on the number of finite elements used.

6. Results and discussion

The computational models described above may be employed to predict the electric field distribution, electric pressure distribution along the surface of a droplet, droplet shapes, transient full-3-D temperature distribution and internal convection in the droplets driven by surface tension force. Extensive numerical simulations have been carried out for various heating conditions. A selection of computed results is given below. The thermophysical properties used for calculations are tabulated in Table 1. The criterion for the convergence of non-linear iteration is set to 1×10^{-4} (norm-2 relative error).

6.1. Mesh selection and mesh independency test

The mesh independence testing procedure for droplet deformation calculations has been discussed in previous publication [11,12] and thus omitted here. Numerical tests show a total of 48 linear boundary elements were

Table 1
Parameters used in calculations

Parameters	Values
T_{melt} (K)	1940
Q_0 (W/m^2)	1.3×10^6
a_d (mm)	2.5
ρ (kg/m^3)	4110
μ (kg/m s)	5.2×10^{-3}
γ (N/m)	0.864
$d\gamma/dT$ (N/m K)	-2.6×10^{-4}
K (W/m K)	21.6
C_P (J/kg K)	700
E (V/m)	3.3×10^6
Emissivity ε_0	0.3
β (K^{-1})	6.5×10^{-6}
Pr	1.685×10^{-1}
a_l (mm)	2.05

adequate for the electric field calculations and 24 quadratic boundary elements for the computation of free surface deformations. The thermal and fluid flow calculations used 8-node hexahedral elements. Special treatment is made to generate the hexahedral elements neat the pole. Mesh independence tests for flow and thermal simulations were conducted such that the numerical error in two consecutive mesh refinements is smaller than 0.1% in maximum velocities calculated. From these tests, a mesh of 2900 8-node elements was used for an octant model for the results presented below, which is used to simulate 2- and 4-laser beams, while that of 3680 8-node elements for a one-third model, to take advantage of symmetry associated with the heating arrangement. Other meshes were also used and tested for mesh independence for other laser heating conditions. Some typical meshes used for 3-D thermal and fluid flow calculations are shown in Fig. 3. Meshes for droplet deformation and 2-D models were given in previous publications [11–13].

6.2. Droplet deformation

For a majority of microgravity experiments, the droplet deformation is determined primarily by the balance of the surface tension and electric stresses long the surface, and the contribution of the hydrodynamic and viscous stresses is negligible, typically on the order of 1% [12,13]. Thus, for these cases, the computation of the droplet deformation can be decoupled from the fluid flow calculations. Also, experiments show that under normal conditions considered for space applications, the droplet deformation is axisymmetric.

In microgravity, the electric forces are designed to position the droplet in a designated location. As a net lifting force is not needed, the total net charge is equal to zero. However, as the droplet is placed in the electric field, the perturbed field induces surface charges on the

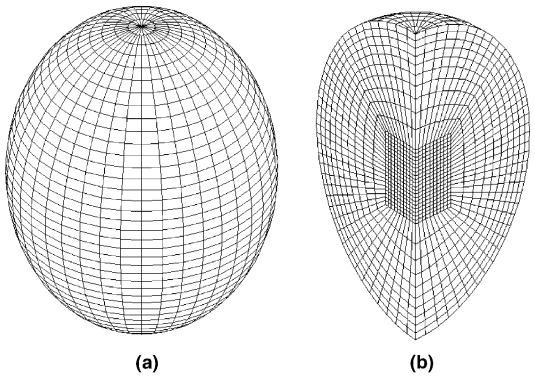

Fig. 3. Finite element meshes for 3-D computations.

droplet. These induced surface charges interact with the imposed electric field to ensure that the electric field inside the droplet is zero and that the entire droplet is kept at a constant potential. While the net force is zero, the local electric force along the surface is not, which must be balanced by the surface tension force, thereby defining the free surface profile for the droplet. Fig. 4 shows the result of surface deformation obtained from the hybrid finite/boundary model. Because the surface charges are negative on the lower half surface and positive on the upper half surface, they combine with an upward electric field to produce a force that pulls the surface outward from the center. Moreover, the surface charges are symmetrically distributed due to the symmetry of the applied electric field, which causes the droplet to deform symmetrically. To satisfy the mass conservation, the droplet is squeezed at the equator, resulting in the shape as shown.

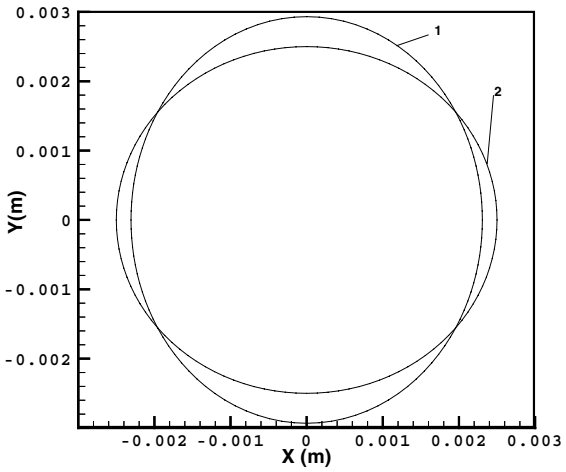

Fig. 4. Comparison of free surface profiles of an electrically conducting droplet in normal and microgravity: (1) $E_0 = 3.3\times10^6$ V/m and $Q = 0$ C, and (2) un-deformed liquid sphere.

It is noteworthy that an electrostatic field in general produces a potential apex that is intrinsically unstable for the purpose of levitation. As a result, delicate dynamic control system is required to make the levitation operation feasible. This is in contrast with induction principle, which produces a potential wall for intrinsically stable electromagnetic levitation.

6.3. Steady-state fluid flow and temperature distribution

As stated before, the only non-zero Maxwell stress component on an electrically conducting droplet is normal to the droplet surface in the natural coordinate, which contributes to droplet deformation only. Therefore, the fluid flow in the droplet is caused by the surface tension variation along the surface only, which in turn stems from a non-uniform temperature distribution created by laser heating. While any types of heating arrangements can be simulated with the numerical model described above, we consider below four different types that are either used in practice or being considered for use in the near future. These heating arrangements give rise to a complex 3-D flow structure, except an axisymmetric placement of heating lasers.

6.3.1. One laser beam on a pole or equator

Early practice of heating the sample in an electrostatic levitator is to apply one laser beam at either the equator or one of the poles. When the laser beam is directed at the pole, the flow field and temperature distribution are axisymmetric and thus a 2-D model is sufficient to describe the transport phenomena. This 2-D model was reported in early studies [11,12] and here it serves as a check on the 3-D model. The 3-D model uses a quarter model consisting of a slice cut by two planes intersecting long the z-axis. The comparison of the previous 2-D model and the present 3-D model results indicates that the two produce the same flow pattern and agree within 0.1% (relative error) in maximum velocities calculated, verifying that the 3-D model indeed reproduces the asymmetric model results (see Fig. 5(a) and (b)). Other meshes, such as whole sphere and half sphere were also used for additional testing and the same conclusions were held.

When the laser is directed at the equator, however, the flow and temperature distributions are no longer strictly axisymmetric. This is because the sample, after deformation, does not possess a rotational symmetry with respect to either the x- or y-axis. However, the fields are of four-fold symmetry with respect to the y–x-plane and x–z-planes. This symmetry condition permits the use of another quarter model, which is a quadrant formed by the y–x-plane and x–z-planes, when the laser beam is applied along the x-axis. The calculated results of the steady-state thermal and fluid flow fields are shown in Fig. 5(c) and (d). Inspection of the results

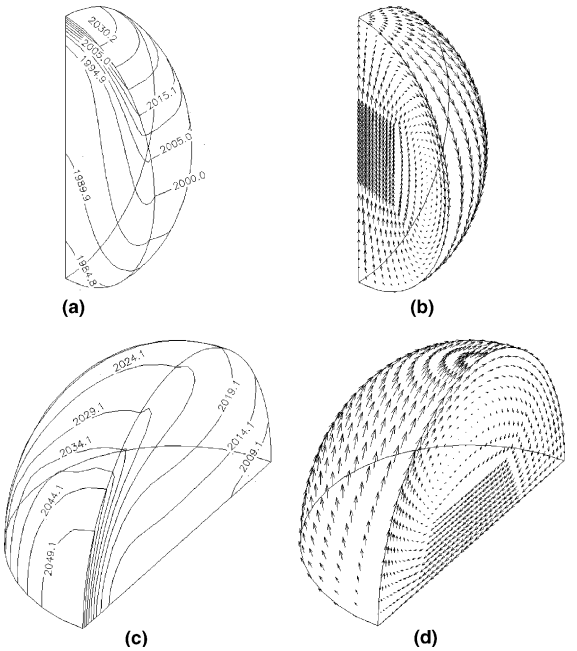

Fig. 5. Temperature distribution and internal fluid flow in an electrostatically deformed droplet under microgravity with a single beam heating laser: (a, b) for single beam placed at the north pole—U max = 14.64 cm/s and (c–d) for single beam placed at the equator—U max = 14.43 cm/s. Heat flux $Q_0 = 2.6 \times 10^6$ W/m^2.

suggests that the flow and temperature distributions head at the pole and equator are very similar. And even the temperature difference and velocity are nearly the same (with <0.1%). Thus, for 1-beam heating configuration, the thermal and flow fields are not strongly affected by the placement of the laser heating source, and flow is characterized by a single recirculating loop in a plane cutting through the x-axis. Further simulations show that unless the deformation is large, this conclusion remains true.

These simple flows are also illustrative of the underlying physical principles governing the Marangoni flow in the droplet. As the droplet is heated up, the temperature is higher within the laser beam coverage and decreases away from the heating center. The steady-state thermal field is established eventually when the radiation and heating are balanced. This non-uniform temperature distribution causes a change in surface tension so as to establish a surface force gradient on the droplet. For the case under study, the surface tension force increases with decreasing temperature. Consequently, the higher force pulls the fluid particles away from the low force region and moves them along the surface from high to low temperature region, where flow moves inward to form a recirculating loop in compliance with the mass continuity requirement.

6.3.2. Two laser beams on the poles or equator

The use of two laser beams to heat the sample is also practiced. The two possible laser beam arrangements are such that the beams are either applied at the two poles, which give rise to a symmetric field distribution, or at the two opposite side of the equator. For the former, a 2-D model is adequate [12], and thus provides once again a checkpoint against which the 3-D model is tested. Computed results confirm that the 2-D and 3-D model predictions are indeed in perfect agreement when the laser beams are applied at the two pole. A 3-D view of the thermal and flow fields is presented in Fig. 6(a) and (b). The two-dimensional, axisymmetric flow structure is well predicted by the 3-D model, as is expected. The temperature is higher at the poles and decreases towards the equator. This establishes a surface force gradient by which the fluid particles are pulled towards the equator at low temperature from the two poles that are at higher temperatures. This, combined with the requirement of mass conservation, generates the double toroidal recirculating flow loops.

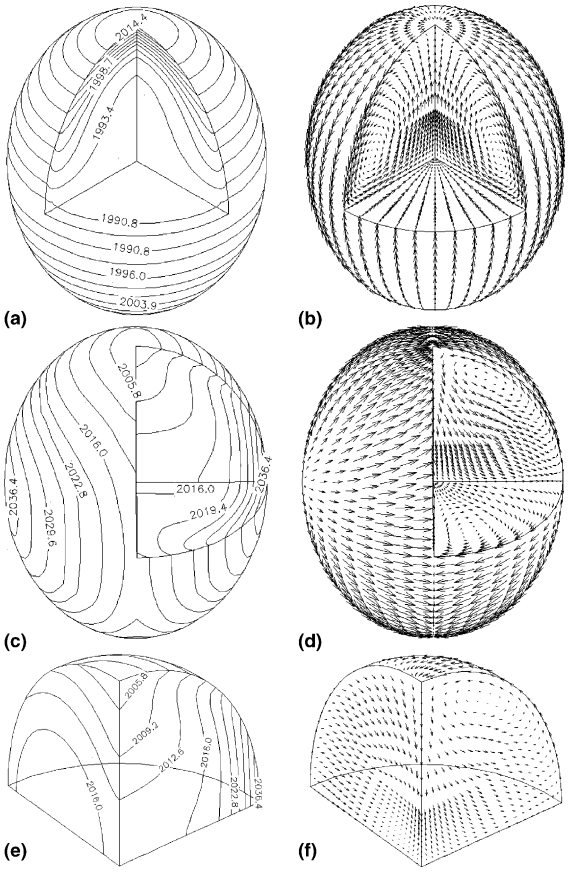

Fig. 6. Temperature distribution and internal fluid flow in an electrostatically deformed droplet under microgravity with heating by dual lasers: (a, b) for beams placed at north pole—U max = 10.98 cm/s and (c–f) for beams placed at the equator—U max = 11.59 cm/s. Heat flux $Q = 1.3 \times 10^6$ W/m^2.

To compare, two laser beams are applied symmetrically on the equator. The radius of the laser beams is the same in the two cases. Strictly speaking, surface deformation precludes the use of the rotational symmetry condition; but the 8-fold symmetry is still applicable. As a result, only an octant is required for the calculations. The computed results, showing the temperature and fluid flow distributions both on the surface of and inside the droplet, are presented in Fig. 6(c)–(f).

Comparison of the results in Fig. 6 reveals that the flow structures and temperature distributions are similar for both cases. Detailed analyses, however, uncovers that the rotational flow loop is only approximately symmetric around the axis formed by connecting two heating sources applied at the equator, which is consistent with the geometric constraint. Further numerical simulations show that a rotational symmetric flow field is obtained if a droplet of perfect sphericity is heated with the two heating sources placed at the two opposite sides of the equator. From Fig. 6, it is seen also that the internal convection has a strong effect on the temperature distribution, which is suggested by the distorted isothermal contour lines. For these two cases, the temperature difference is 28.8 and the maximum velocity is 10.978 in the case of pole heating, which compares 37.4 and 11.592, respectively, for the equator heating. Further simulations show that with the same Q_0 and same radius of laser beams applied at the equator, the average temperature is about 20 K higher than heating at the poles, but the temperature difference and hence the maximum velocity is roughly the same as those in Fig. 6(a) and (b).

6.3.3. Tetrahedral heating by four laser beams

Recently, there have been strong advocates in the droplet levitation community for the use of a tetrahedral laser beam heating arrangement as a potential means to reduce the temperature gradient in the droplet, thereby reducing the internal convection. In this arrangement, four parts of the droplet surface are heated by lasers beams that are emitted from the four corners of a tetrahedron whose geometric center is coincident with that of the droplet. This design concept may be explored using the 3-D model before expensive instrumentation is put in place, which in essence is the usefulness of a numerical model. Because of the tetrahedral arrangement, symmetry conditions can be applied on the plane that cuts through the two poles and the center of a laser beam placed around the droplet. Thus a 1/3 model is sufficient to represent the complex flow and temperature field in the droplet. The model used 3600 8-node finite element elements.

The calculated results are depicted in Fig. 7. Clearly, tetrahedral heating creates a rather complex flow structure, with fluid moving from four high temperature

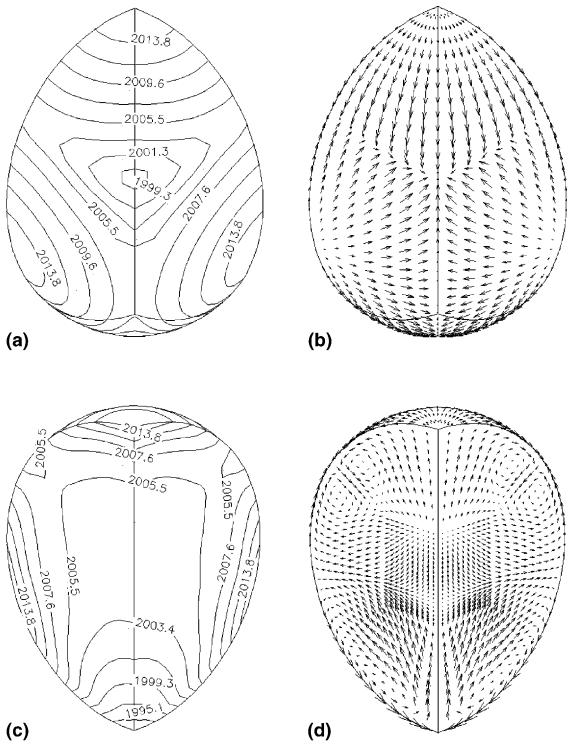

Fig. 7. Steady-state thermal and velocity fields in an electrostatically deformed droplet under microgravity with tetrahedral heating arrangement: U max = 9.728 cm/s. $Q = 0.65 \times 10^6$ W/m^2.

regions to the low temperature regions (see Fig. 7(a) and (c)). The complexity of fluid motion is further revealed by the internal flows shown in Fig. 7(b) and (d). The four hot spots are apparently associated with the laser heating and flows emerge from these hot spots to find their ways to the regions where temperatures are low, as a result of surface forces increasing with a decrease in temperature. Again, the internal flow recirculation produce a strong effect on the temperature distribution, as is evident in the isothermal contour plots viewed in slice cuts (Fig. 7(a) and (c)).

Comparison of Figs. 6 and 7 exhibits that a tetrahedral heating arrangement, though produces a more complex internal flow field, indeed gives a more much uniform temperature distribution inside the droplet: a temperature difference of 22.9 for tetrahedral heating vs. that of 28.8 for dual laser heating. In sharp contrast with the common perception, the maximum velocity generated by the tetrahedral heating is not reduced significantly in accordance with the temperature reduction. In fact, only a small reduction of velocity (11%) is observed. This result, which is contradictory to what is anticipated by 4-beam advocates, may be explained as follows. While the temperature difference indeed is much smaller with 4-laser beams than with 2-beams, the temperature gradient along the surface is not as much different between the two cases, thereby resulting in a reduction of velocity only by 11%. Detailed analyses further show that for the 2-beam cases, the temperature gradient between the hottest and coldest spots on the surface is 7.334×10^3, which compares with 7.143×10^3 for 4-beam lasers.

For surface tension driven flows, the Marangoni number is often used as an indicator of flow intensity. For electrostatically levitated droplets under consideration, however, one can not use the Marangoni number based on a single characteristic length (say, radius) to interpret the flows resulting from different heating arrangements for levitated droplets, though it is legitimate for the same heating configuration. This is because the length scales are different for different heating configurations, as discussed in the paragraph above. A correct use of Marangoni numbers to characterize the flows must take into the consideration the length scale changes for different heating arrangements.

6.3.4. Heating by six laser beams

Besides the dual and tetrahedral laser beam arrangements, other heating placements can also be investigated using the numerical model described above. One of the viable arrangements would be to use a 6-beam laser heating arrangement, symmetrically placed with respect to the center of the droplet, for the purpose of further reducing the temperature non-uniformity and a hope for a smaller flow velocity. One possible arrangement is to split the laser heating source into six laser beams, which will allow heating to be applied equally on octahedrons of a droplet.

One such calculation is given in Fig. 8, where the 6-laser beams are arranged such that two are at the poles and 4-beams are placed around the equator plane with equal spacing, which are distributed at the 6 corners of the octahedron. Compared with the 2-laser beams' case, the calculated results indicate that the surface temperature gradient is reduced by about 50% and so is the internal velocity with this arrangement. This is consistent with the above analysis in that a surface thermal gradient reduction results in a decrease of the Marangoni flow. A detailed inspection of these flow structures, although very complex, seems to suggest that these complex flow structures are a result of interaction of the Marangoni flow cells associated with each laser beams.

A summary of major results calculated for different heating arrangements is given in Table 2. The results should serve as a rational guide and the model would be a useful tool for selecting conditions for levitated droplet studies. For example, for applications demanding a low flow condition and a more uniform temperature distribution, either more beams or large beam diameter or a combination of the two are needed. The effect of the beam sizes and laser intensity on flow and temperature

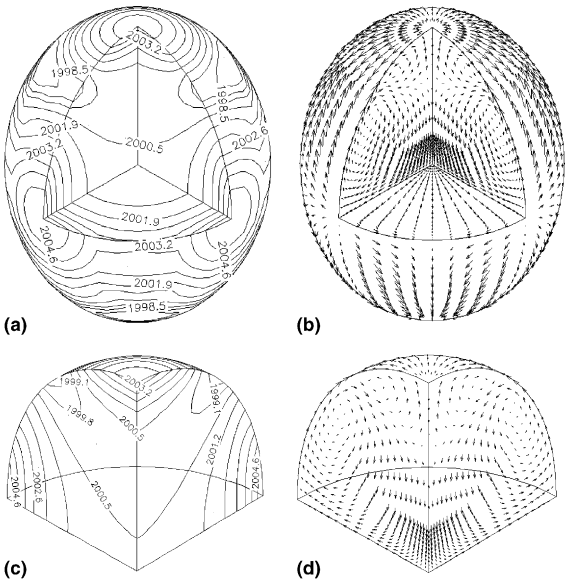

Fig. 8. Steady-state thermal and velocity fields in an electrostatically deformed droplet under microgravity with octahedral heating arrangement: U max = 5.321 cm/s. $Q = 1.3 \times 10^6/3$ W/m^2.

distributions is discussed elsewhere [11,12]. Further calculations show that for the cases where the flow intensity is very low because of the smaller surface temperature gradient, the effect of convection is minimized and the temperature distribution becomes similar to that in a solid sphere, as expected. For these cases, however, the convective flow structure remains the same as discussed above, that is, it is determined by the heating source arrangements.

6.4. Transient development of flow and thermal fields

For undercooling studies using the levitated droplets, knowledge of transient flow and thermal fields when heating is turned off is also important. The present 3-D model, like its 2-D counterpart [12], is also capable of describing the transient development of both 3-D fluid flow and temperature distribution in an electrostatically levitated droplet. Figs. 9 and 10 show the time development of 3-D fluid flow and thermal fields in droplets heated by 4- and 6-beam arrangements, respectively. Apparently, the transient fluid flow structure evolves in time differently for the two cases. The transient simulations of axisymmetric thermal and fluid flow fields induced by single and double beams were discussed in a previous paper on 2-D models.

Inspection of Figs. 7 and 9 shows that in the case of the 4-laser beam arrangement, the temperature field changes very rapidly when the heating is turned off, which causes a flow reversal near the north pole region and a change in flow structure in the droplet. At time $t = 0.28$ s after the laser beams are switched off, the surface temperature is largely smeared out due to both convection and radiation such that the temperatures at the north pole is reduced below everywhere, a manifestation of high heat lose there. In three other heating regions, however, the temperature remains relatively higher. This is explained by the fact that for the same laser beam diameter, the surface areas from which heat loss occurs are much smaller because of a much larger surface curvature radius in these regions. Note also that there exists considerable thermal mixing along the azimuthal direction, which brings the temperature into an axisymmetric field. The consequence of this change in thermal fields is that one smaller toroidal loop near the north pool is engulfed by the loop associated with the side heating source. This phenomenon is consistent with the underlying physics governing the surface tension driven flows discussed in Section 6.3.2.

Turning to the time evolution of the thermal and fluid flow fields induced by the 6-beam heating arrangement, one can see that the similar phenomena are observed in that a lower temperature occurs in the polar regions and the temperature is smeared considerably along the azimuthal direction. This is accompanied by the flow change such that the complex flow structure characterized by several recirculating regions is now replaced by basically two large toroidal flow loops recirculating above and below the equatorial plane, as shown in Fig. 10.

To further assess the dynamics of the transient thermal and flow fields, information on the history of velocity and temperature at some specific locations is obtained. Fig. 11 shows the decay of maximum velocities

Table 2
Effects of heat source arrangement on temperature difference and maximum velocity in an electrostatically levitated titanium droplet

Case	T_{high} (K)	T_{low} (K)	$T_{average}$ (K)	ΔT (K)	U_{max} (cm/s)	Re
Two laser heating at two poles	2017.0	1988.2	2002.6	28.8	10.978	216.92
Two laser heating on the equator	2039.8	2002.4	2021.1	37.4	11.592	229.05
One laser heating on northern pole	2035.3	1979.8	2007.55	55.5	14.64	289.28
One laser heating around the equator	2054.1	1999.2	2026.65	54.9	14.43	285.13
Four laser heating on the tetrahedron	2015.9	1993.0	2004.45	22.9	9.728	192.22
Six laser heating on the octahedron	2005.3	1997.8	2001.55	7.5	5.321	105.14

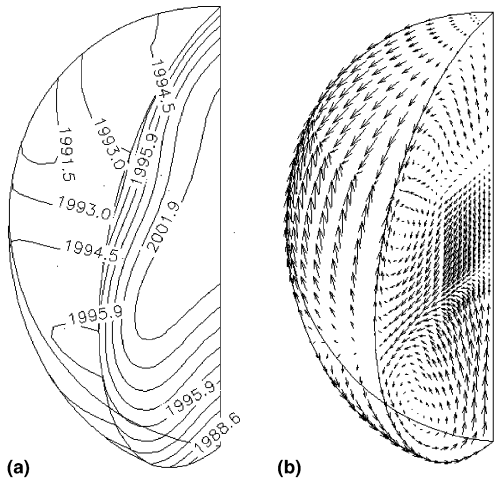

Fig. 9. Snapshots of thermal and melt flow fields during their decay as heating lasers are turned off: (a) temperature distribution and (b) velocity field (U max = 4.376 cm/s) at $t = 0.07$ s, and (c) thermal field and (d) velocity profile (U max = 6.941 cm/s) at $t = 0.28$ s. The initial conditions for the calculations are given in Fig. 7.

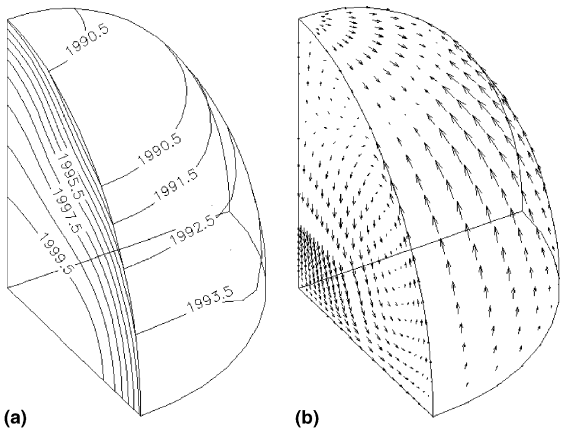

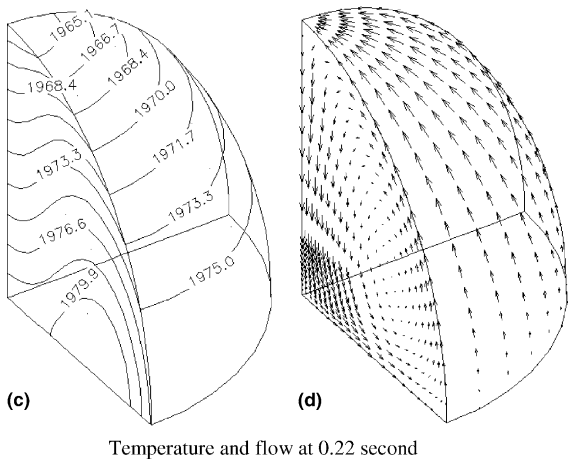

Fig. 10. Snapshots of thermal and melt flow fields during their decay as heating lasers are turned off: (a) temperature distribution and (b) velocity field (U max = 3.812 cm/s) at $t = 0.04$ s, and (c) thermal field and (d) velocity profile (U max = 6.561 cm/s) at $t = 0.22$ s. The initial conditions for the calculations are given in Fig. 8.

and the maximum and minimum temperature differences in the droplet heated by 4- and 6-beams after heating sources are turned off. It is seen that during the first 0.5 s after lasers are shut off, both velocities and temperature differences experience dramatic change and then decay gradually afterwards. After an elapse of 3 s, the maximum velocities reach essentially the same level in the droplet heated initially by either 4- or 6-beams. The maximum velocity changes in accordance with the temperature differences, in compliance with the basic principle of surface tension driven flows. Examination of these transient results along with 3-D views of flow visualization illustrates that the time at which the velocity and temperature spikes up ($t \sim 0.3$ s) corresponds to the time when the internal flow starts to reverse its flow pattern in certain regions, as shown in Figs. 9 and 10.

Although the temperature differences undergo drastic changes, the temperatures at specific locations do not necessarily do so. Typical time change in temperature and velocity at specific locations are compared in Fig. 12 for the droplets heated by 4- and 6-beams. Compared with Fig. 11, these results show that the temperature at the specific point decays more smoothly, although the maximum and minimum temperature differences vary more drastically during the initial transient period. The

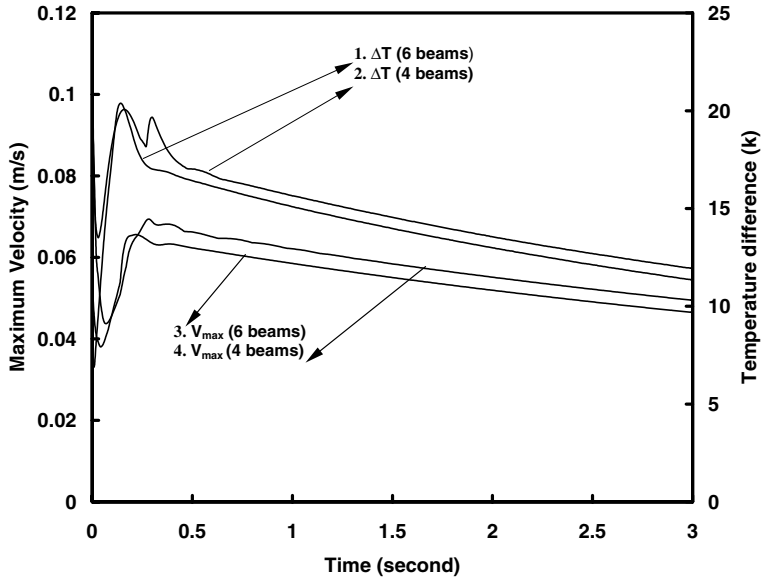

Fig. 11. Decaying history of maximum velocities and the maximum and minimum temperature differences in the droplets heated by 4- and 6-beam heating lasers, after heating is switched off.

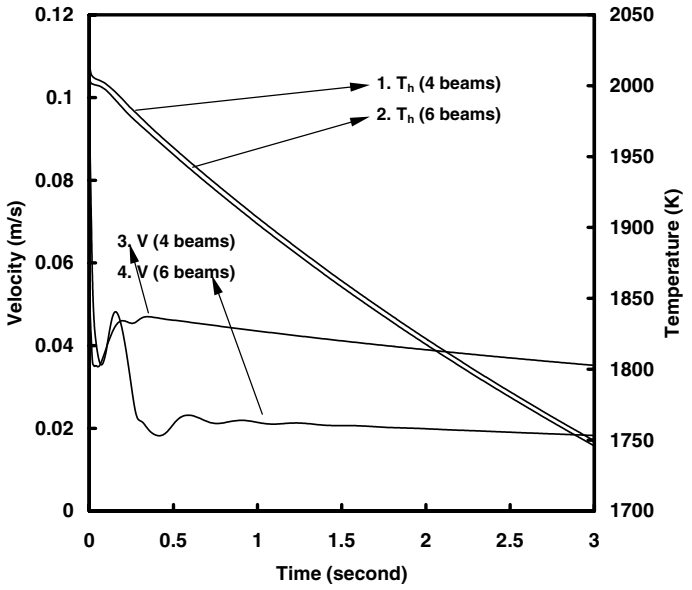

Fig. 12. Transient development of velocities and temperatures at specific points in the droplets heated by 4- and 6-beam heating lasers, after heating is switched off. The velocities are monitored at ($x = 9.3106 \times 10^{-4}$, $y = 5.3755 \times 10^{-4}$, $z = -2.5955 \times 10^{-3}$ all in meters) for 4-beam and at (-2.9974×10^{-4}, 1.8925×10^{-3}, 1.6365×10^{-3}) for 6-beam where the maximum steady-state velocities are attained. The temperatures are monitored at (1.8425×10^{-3}, 1.0638×10^{-3}, -1.1372×10^{-3}) for 4-beam and at (0, 2.3075×10^{-3}, 0) for 6-beam where the maximum steady-state temperatures occur in the droplets.

temperature at this point decreases by about 260 K below the steady temperature or 200 K below the melting temperature. The velocity at the point where the highest steady-state temperature is attained decays very quickly initially and remains approximately constant afterwards.

The evolution of temperature distributions along a line emitting from the center to a point on the droplet surface is plotted in Fig. 13(a) and (b) for 4- and 6-beams heating arrangements, respectively. These results show that the steady-state temperature distribution

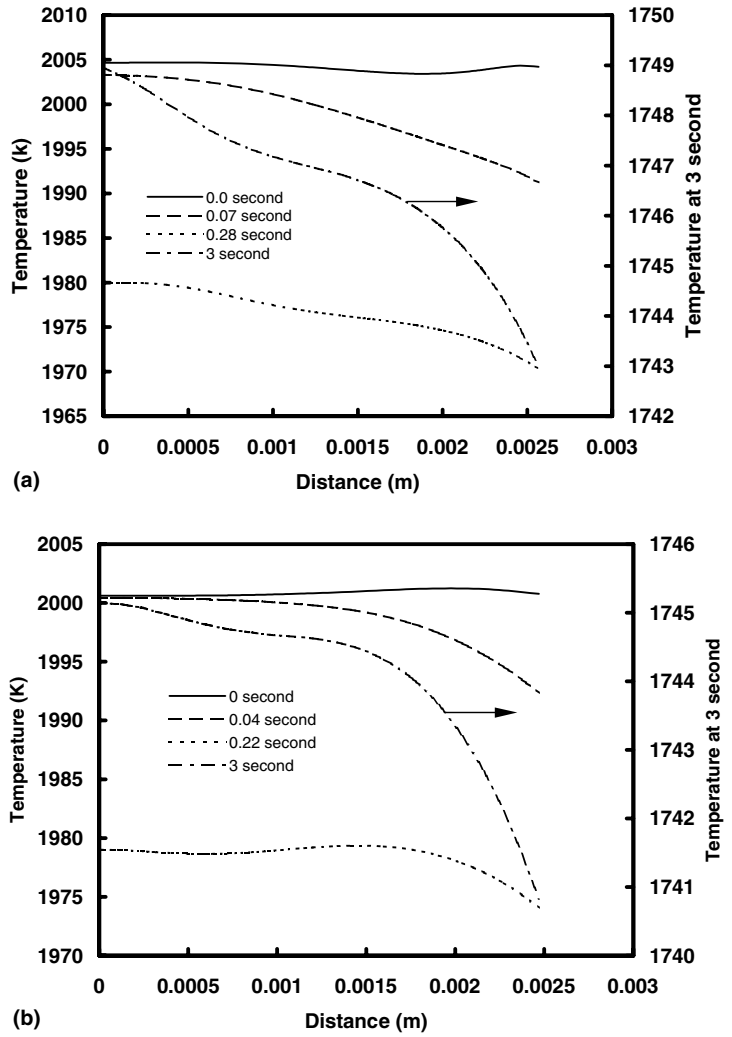

Fig. 13. Evolution of temperature distributions along the line emitted from the center of the droplet to (0,1,1) on the surface for (a) tetrahedral and (b) octahedral heating arrangements. The curve at $t = 3$ s refers to the vertical axis at right.

is rather uniform and as temperature drops, the temperature distribution changes more rapidly. The largest change occurs at around $t \sim 0.25$ s. Note that for clarity of the plots, different scales are used for the temperature distribution at $t = 3$ s, at which time a temperature difference between the center and the surface is $\sim$7 K is obtained for the 4-beam case and $\sim$5 K for the 6-beam case.

With the data given in Table 1, one can show that for this system the time scale for thermal diffusion is about an order smaller than that for momentum diffusion, which is typical for metals. This means that during the transient process the thermal diffusion is much faster than the momentum diffusion. This is clearly suggested also from the results shown in Figs. 11 and 12. Further analysis of the transient results indicates that the transient decaying behavior is very similar to the predictions made using the axisymmetric model, which are discussed in detail in [12]. The local flow structure and temperature distributions, however, are different during the initial transient period, as expected.

7. Concluding remarks

This paper has presented a numerical model for steady-state and transient 3-D Marangoni convection and heat transfer in electrostatically levitated droplets. The numerical model development is based on the Galerkin finite element solution of the Navier–Stokes and energy equations. Numerical aspects for the computation of surface driven flows in general curvilinear

coordinate system have been discussed within the framework of finite elements and differential geometry. Results of droplet deformation by electrostatic forces and both steady-state and transient 3-D Marangoni flows in droplets heated by a variety of heating source arrangements have been presented. For practical microgravity conditions under which the deformation is small, the single and double beam heating arrangements, when placed at the poles (or the equator plane), produce exactly (or approximately) axisymmetric flow profile and temperature distribution with the axis of symmetry defined by the line passing through the centers of the laser beam and the droplet. As such a 2-D axisymmetric model could provide a reasonably good description, and an exact one when placed at the poles. Complex 3-D flow structure emerges when a tetrahedral or octahedral heating arrangement is applied. These complex flow structures result from the interaction of melt flows associated with each laser beam. For the case studied, the tetrahedral heating arrangement does not seem to produce a significant reduction in internal velocity, in contrast to perception, while the temperature is more uniform. This is attributed to the fact that the 2- and 4-beam arrangements result in a surface temperature gradient of approximately the same magnitude. While the Marangoni numbers are able to characterize the flow for a same heating arrangement, a correct use of them needs to factor in the different length scales associated with different heating placements. The six-beam heating placement produces, however, a much more significant reduction in both velocity and temperature non-uniformity. During the transient decaying, both temperature and velocity fields evolve in a complex fashion with the initial stage dominated by the thermal and flow mixing on the surface of a droplet that has been heated by 4- or 6-beam lasers. The flow reversal is also observed in the droplets during the decay, and a spike in velocity and temperature is found at the time when the flow reversal is taken place. The strong surface mixing quickly brings out a surface temperature distribution of axisymmetry, while inside the droplet the 3-D structure still persists until much later.

Acknowledgements

Financial support of this work by the NASA Microgravity Science and Applications Division (Grant #: NAG8-1477) is gratefully acknowledged.

References

[1] J.W.S. Rayleigh, On the equilibrium of liquid conducting mass charged with electricity, Philos. Mag. 14 (1882) 184.
[2] J.R. Reitz, F.J. Milford, R.W. Christy, Foundations of Electromagnetic Theory, Addison-Wesley, Reading, MA, 1979.
[3] S. Torza, R.G. Cox, S.G. Mason, Electrohydrodynamics deformation and burst of liquid drops, Philos. Trans. R. Soc. London A 269 (1971) 295.
[4] P.M. Adornato, R.A. Brown, Shape and stability of electrostatically levitated drops, Proc. R. Soc. London A 389 (1983) 101–117.
[5] J.Q. Feng, K.V. Beard, Small-amplitude oscillations of electrostatically levitated drops, Proc. R. Soc. London A 430 (1878) (1990) 133.
[6] J.R. Melcher, Continuum Electromechanics, MIT Press, Cambridge, Mass, 1981.
[7] S.S. Sadhal, E.H. Trinh, P. Wagner, Thermocapillary flows in a drop with unsteady spot heating in a microgravity environment, J. Microgravity Sci. Tech. 9 (2) (1996) 80.
[8] W.K. Rhim, Thermophysical property measurements of molten semiconductors, in: NASA Microgravity Materials Science Conference, Huntsville, AL, USA, 1997, p. 427.
[9] S.P. Song, B.Q. Li, Coupled boundary/finite element analysis of magnetic levitation processes: free surface deformation and thermal phenomena, J. Heat Transfer 120 (1998) 492–504.
[10] B.Q. Li, S.P. Song, Thermal and fluid flow aspects of magnetic and electrostatic levitation of liquid droplets, J. Microgravity Sci. Tech. XI (4) (1999) 134–143.
[11] S.P. Song, P. Dailey, B.Q. Li, Effects of heating source arrangements on internal convection in electrostatically levitated droplets, AIAA J. Thermophys. Heat Transfer 14 (3) (2000) 335–362.
[12] S.P. Song, B.Q. Li, Free surface shapes and thermal convection in electrostatically levitated droplets, Int. J. Heat Mass Transfer 43 (2000) 3589–3606.
[13] S.P. Song, B.Q. Li, A hybrid boundary/finite element method for simulating viscous flows and shapes of droplets in electric fields, Int. J. Comput. Fluid Dyn. 15 (2001) 293–308.
[14] C.E. Weatherburn, Differential Geometry of Three Dimensions, Cambridge University Press, Fetter Lane, London, 1930.
[15] M.S. Engelman, R.L. Sani, P.M. Gresho, The implementation of normal and tangential velocity boundary conditions in finite element codes for incompressible fluid flow, Int. J. Numer. Meth. Fluids 2 (1982) 225–238.
[16] I.S. Duff, J.K. Reid, The design of MA48, a code for the direct solution of sparse unsymmetric linear systems of equations, ACM Trans. Math. Software 22 (2) (1996) 187–226.